Geophysical Prospecting EAGE EUROPEAN ASSOCIATION OF GEOSCIENTISTS & ENGINEERS
Geophysical Prospecting, 2020, **68**, 2347–2360 doi: 10.1111/1365-2478.12997

Optimum size and density of surface grid arrays for retrieving accurate shear-tensile fracturing of microearthquakes

Yi Ren[1], Yongtao Gao[1], Shunchuan Wu[1,2] and Václav Vavryčuk[3]*
[1]*Key Laboratory of Ministry for Efficient Mining and Safety of Metal Mines, University of Science and Technology Beijing, Beijing 100083, China,* [2]*Land Resources Engineering, Kunming University of Science and Technology, Kunming Yunnan 650093, China, and* [3]*Institute of Geophysics, The Czech Academy of Sciences, Boční II/1401, Praha 4, 14131, Czech Republic*

Received February 2019, revision accepted June 2020

ABSTRACT
Surface arrays became an important tool for monitoring the induced seismicity in hydraulic fracturing experiments and for assessing the impact of fluid injection on the fracturing process of microearthquakes. The layout of sensors plays a key role in this task because it controls the accuracy of event locations and retrieved seismic moment tensors. We simulate various configurations of grid sensor arrays characterized by a different number of sensors, array span, sensor spacing, depth of sources and various shear/tensile source mechanisms of events. The moment tensor inversion is carried out using synthetically calculated P-wave amplitudes with added random noise. A bias in the solutions is evaluated by errors in the double-couple percentage of inverted moment tensors because the double-couple errors inform us about the sensitivity of the network to detect the shear/tensile fracturing mode of induced microearthquakes. The results show that the accuracy of the double-couple percentage is mostly controlled by the offset-to-depth ratio R defined as the ratio of half of the network size to the event depth. The optimum value of R is in the range of 0.75–1.5 irrespective of the type of the focal mechanism. If 121 (11×11) sensors are distributed in a regular grid and recorded data are characterized by a 10% random noise, the double-couple error is less than 6%. This error increases, if R is not optimum or if the number of sensors is reduced. However, even sparse arrays with 49 (7×7) or 16 (4×4) sensors can yield a reasonable accuracy, provided the surface grid arrays are designed to have an optimum size.

Key words: Acquisition, Inversion, Monitoring, Passive method, Seismics, Surface monitoring.

INTRODUCTION

The surface and near-surface arrays are an important part of microseismic monitoring in hydraulic fracturing experiments. The surface monitoring has many inherent advantages: (1) It can provide a dense azimuthal coverage; (2) it is significantly more cost-effective as there is no need to drill observation wells and deploy sensors specifically designed for the operation in wells (Duncan, 2005; Vavryčuk, 2007) and (3) it permits deployments of much more instruments than for arrays installed in wells (van der Baan *et al.*, 2013). Consequently, the surface monitoring is an efficient tool for a high-resolution imaging of microseismicity and for the determination of accurate parameters of microseismic events including their locations and fracturing mode.

Several authors have investigated the accuracy of locations and moment-tensor solutions of events induced by hydraulic fracturing monitored by various layouts of the surface

*E-mail: vv@ig.cas.cz

© 2020 The Authors. *Geophysical Prospecting* published by John Wiley & Sons Ltd on behalf of European Association of Geoscientists & Engineers.
This is an open access article under the terms of the Creative Commons Attribution-NonCommercial License, which permits use, distribution and reproduction in any medium, provided the original work is properly cited and is not used for commercial purposes.

Table 1 Summary of applications of surface microseismic monitoring systems

Time	Author	Receiver Number	Receivers Span (m)	Receivers Layout	Event Depth(m)	Research Goal
2005	Duncan	100	2000-3000	Uniform	2300	Comprehensive research
2009	Vernier *et al.*	225	2800	Uniform	2100	Location
2009	Eisner *et al.*	121	6000	Uniform	3000	Location
2009	Šílený	23	About 10,000	Nonuniform	5250	MTI
2010a	Eisner *et al.*	773	4000-5000	Star	2200	Location
		121	6000	Uniform	3000	Location
2010b	Eisner *et al.*	980	3000-4000	Star	1800	MTI
2010	Chambers *et al.*	800	About 6000	Star	3000	Location
2010	Duncan and Eisner	97	About 2500	Uniform	2400	Comprehensive research
		1428	About 6000	Star	Unclear	Comprehensive research
		980	3000-4000	Star	1800	Comprehensive research
2011	Eaton and Forouhideh	82	4000	X	3000	MTI
2011	Thornton and Eisner	1000	About 8000	Star	3000	Location
2011	Wessels *et al.*	206	About 12,000	Uniform	4000	MTI
2011	Zhang *et al.*	100	8100	Uniform	3780	Location
2013	Van Der Baan *et al.*	29	About 2000	Nonuniform	2000	Comprehensive research
2013	Jansky *et al.*	25	1150	Uniform	1125	Location
2013	Kushnir *et al.*	150	About 3500	Nonuniform	1870	Location
2014	Staněk *et al.*	911	About 5000	Star	2100	MTI
		99	10,000	Uniform	4000	MTI
2014	Anikiev *et al.*	911	About 5000	Star	1700–2100	Location and MTI
2016	Pesicek *et al.*	178	about 5000	Uniform	800–1300	MTI
2017	Staněk *et al.*	800	5000	Star	2300	MTI
		104	About 2000	Uniform	300–700	MTI
2017	Eyre and van der Baan	73	1800	Star	1000	MTI

Note: MTI means the moment tensor inversion.

monitoring systems (see Table 1). For example, Šílený (2009) studied the accuracy of the moment tensor (MT) inversion assuming a varying number of sensors. Staněk *et al.* (2014) analysed effects of seismic noise and velocity models with varying geometry of the sensor deployment in the surface and near-surface monitoring. Eyre and van der Baan (2017) studied effects of varying locations of events at the same depth monitored by receivers with a fixed layout. In summary, the authors showed that the accuracy of event locations and retrieved MTs strongly depend on the number of sensors and the sensor layout. Consequently, a careful arrangement of the sensor arrays is essential for determining accurate source parameters of induced microseismic events in all field experiments.

In this paper, we study the accuracy of seismic MTs determined by a different number and spacing of sensors arranged in a regular grid. We consider various depths of events and source mechanisms. Using numerical modelling, we simulate realistic conditions in field experiments by considering noise in data and errors in event locations. We focus on the problem, how to configure a cost-effective surface network of sensors to achieve a desired accuracy of the double-couple (DC) percentage of the MTs, which informs us about the shear-tensile character of fracturing mode of induced microearthquakes. This knowledge is particularly important for understanding the physics of fracturing in the fluid-induced seismicity.

METHOD

The seismic moment tensors (MTs) are commonly determined using the following three methods: the first-arrival polarity inversion, the amplitude inversion and the full-waveform inversion (Eyre and van der Baan, 2015; Vavryčuk *et al.*, 2017). The advantages and disadvantages of the three methods can be summarized as follows: (1) The first-arrival polarity inversion is simple and fast to be implemented but also it is crude, likely producing the least reliable results. (2) The full-waveform inversion can provide results of a very good quality, including source-time functions but involves much more complex and expensive calculations and relies on accurate seismic velocity models. (3) The amplitude inversion is simple but still a very powerful method, which is applicable even to complicated 3D structures, if Green's functions are calculated by the ray theory

(Červený, 2001). The amplitude inversion was recommended and cited by many authors (Mahdevari *et al*., 2016; Vavryčuk *et al*., 2017; Bentz *et al*., 2018; McLaskey and Lockner, 2018).

Considering complexities in the propagation of S waves, which are more sensitive to small-scale inhomogeneities (Kühn and Vavryčuk, 2013) and to seismic anisotropy because of shear-wave splitting, S-wave triplications, singularities and caustics (Vavryčuk, 1997, 2003a, 2003b), we adopt the P-wave amplitude inversion to study the simulated events. This approach proved to be robust and rather insensitive to an inaccurately known velocity model (Šílený and Vavryčuk, 2000, 2002; Stierle *et al*., 2014a, 2014b). For the inversion, we utilize the 'Focimt' code, a free software provided by Kwiatek *et al*. (2016). The software has been applied to hydraulic fracturing data (Martínez-Garzón *et al*., 2016), induced seismicity in geothermal fields (Bentz *et al*., 2018) and in mines (Rudziński *et al*., 2017; Zhao *et al*., 2018), or to laboratory data (McLaskey and Lockner, 2018).

The MT inversion is based on the following formula:

$$\mathbf{u} = \mathbf{G}\mathbf{M}, \tag{1}$$

where $\mathbf{G}$ is the $N \times 6$ matrix of Green's function derivatives, representing the response of the medium along the ray path between the sensor and the source; $\mathbf{u}$ is the $N \times 1$ vector, representing the observed displacement at the sensors and N is the number of amplitude observations. The 1×6 vector $\mathbf{M}$ contains six independent MT components, which describe geometry of fracturing at the source.

For simplicity, we assume homogeneous isotropic media, which were proved to be a good approximation in P-wave studies of the local microseismicity, where rays are close to straight lines and their take-off angles from the source do not significantly deviate from those in the homogeneous medium (Červený, 2001; Onnis and Carcione, 2017; Eide *et al*., 2018). This condition is not valid for near-surface sources such as explosions with depth less than 100 m (Růžek *et al*., 2003; Vavryčuk, 2008), which are not considered here. The microseismic events are described by angles: strike, dip, rake and slope (Vavryčuk, 2001, 2011). The strike, dip and rake angles describe the standard shear mechanism; the slope angle (also called the tensile angle) characterizes tensile or compressive events and defines the angle between the slip vector and the fault plane. The synthetic P-wave amplitudes are calculated using the formula presented in Ou (2008) and Kwiatek and Ben Zion (2013). The P-wave amplitudes are contaminated by noise and inverted for MTs. The difference between the original and retrieved MTs serves as a measure of errors introduced by the inversion.

The MTs are further decomposed according to Vavryčuk (2001, 2011) into the isotropic (ISO), double-couple (DC) and compensated linear vector dipole (CLVD) components, and their errors due to inversion are analysed. The MT is decomposed as follows:

$$\mathbf{M} = \mathbf{M}^{\mathrm{ISO}} + \mathbf{M}^{\mathrm{DC}} + \mathbf{M}^{\mathrm{CLVD}} \tag{2}$$

with

$$\mathbf{M}^{\mathrm{ISO}} = \frac{1}{3}\mathrm{tr}\,(\mathbf{M}) \begin{bmatrix} 1 & 0 & 0 \\ 0 & 1 & 0 \\ 0 & 0 & 1 \end{bmatrix} \tag{3}$$

$$\mathbf{M}^{\mathrm{CLVD}} = |\varepsilon|\, M^{*}_{|\max|} \begin{bmatrix} -1 & 0 & 0 \\ 0 & -1 & 0 \\ 0 & 0 & 2 \end{bmatrix} \tag{4}$$

$$\mathbf{M}^{\mathrm{DC}} = (1 - 2\,|\varepsilon|)\, M^{*}_{|\max|} \begin{bmatrix} -1 & 0 & 0 \\ 0 & 0 & 0 \\ 0 & 0 & 1 \end{bmatrix} \tag{5}$$

$$\varepsilon = -\frac{M^{*}_{|\min|}}{\left|M^{*}_{|\max|}\right|}, \tag{6}$$

where $\mathbf{M}^{\mathrm{ISO}}$ stands for the ISO component, $\mathbf{M}^{\mathrm{DC}}$ is the DC component and $\mathbf{M}^{\mathrm{CLVD}}$ is the CLVD component. The sum of the ISO and CLVD components is called the non-DC component of $\mathbf{M}$. $M^{*}_{|\max|}$ and $M^{*}_{|\min|}$ are the eigenvalues of the deviatoric moment with the maximum and minimum absolute values, respectively. The ISO, DC and CLVD components are further normalized and evaluated in percentages; for details see Vavryčuk (2001). For pure shear events, the DC component is 100%. For pure tensile or compressive events, the DC component is zero.

SIMULATION

Here we assume an array with sensors evenly distributed in a square and the source located below its centre (see Fig. 1). The offset-to-depth ratio R is defined as

$$R = b/\left(2d\right), \tag{7}$$

where b is the array span and d is the depth of the source. The layout of sensors is 11×11, with spacing a of 100, 300, 600 and 900 m. The depth of simulated events is 1000, 1500, 2000, 2500, 3000, 3500, 4000 and 4500 m. Different ratios R corresponding to different working conditions are shown in

© 2020 The Authors. *Geophysical Prospecting* published by John Wiley & Sons Ltd on behalf of European Association of Geoscientists & Engineers.,

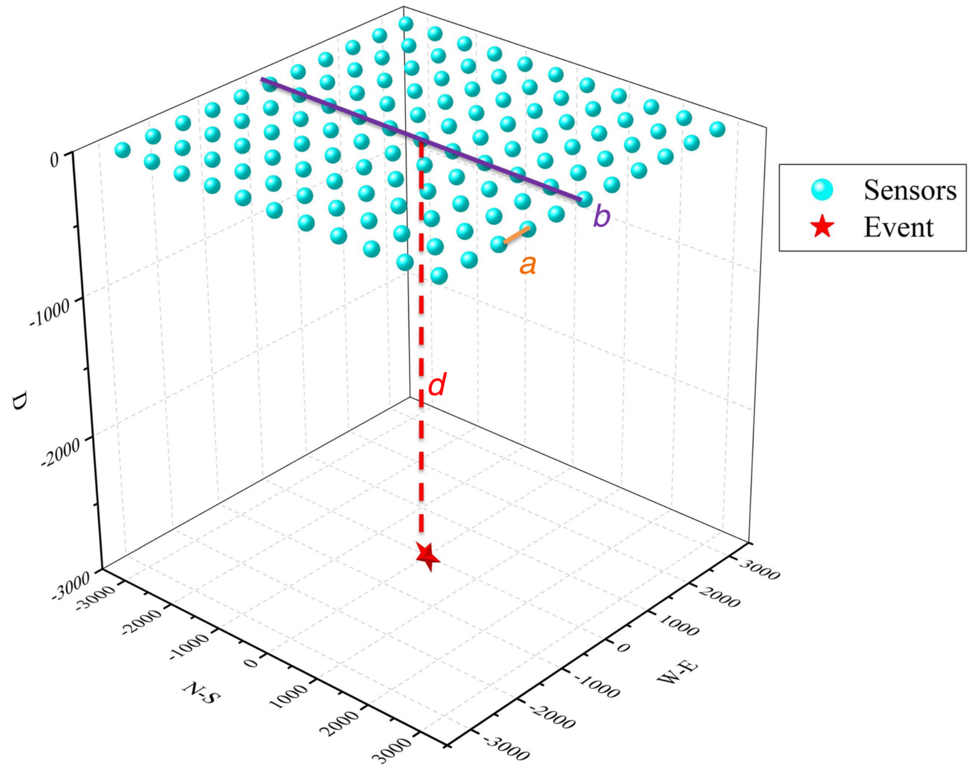

Figure 1 Schematic diagram of the sensor layout: *a* is the sensor spacing; *b* is the array span; *d* is the event depth.

Table 2. The layouts of sensors projected on the focal sphere are shown in Fig. 2. Since seismic noise might have a great impact on the surface recordings, we add random noise with a flat probability distribution between −10% and +10% of the maximum amplitude recorded by the sensor array. In this way, we mimic a situation when all sensors are affected by the same level of seismic noise. Consequently, the traces with large P-wave amplitudes have a high signal-to-noise ratio (SNR), while the traces recording small amplitudes near the nodal lines have a low SNR. For the simplicity, we do not consider variations of the SNR with the focal mechanism or with depth of the event.

In order to ensure a comprehensive and stable analysis, 500 random simulations are conducted for each configuration. Mostly, events with arbitrarily varying strike (0°–360°), dip (0°–90°) and rake (−180° to 180°) angles are simulated. As the strike-slip event (with strike 45°, dip 90° and rake 0°) and the dip-slip event (with strike 45°, dip 90° and rake 90°) were often studied by other authors (Maxwell *et al.*, 2010; Wessels *et al.*, 2011; Staněk *et al.*, 2014; Eyre and van der Baan, 2017), we also simulated events with these two special focal mechanisms to check whether the results deviate from those for the events with a random focal mechanism. The slope angles α are assumed to be 0°, 10°, 30° and 90°, respectively.

Table 2 The offset-to-depth ratios *R* for different sensor spacing and event depths

	Event depth *d*							
Spacing *a*	1000 m	1500 m	2000 m	2500 m	3000 m	3500 m	4000 m	4500 m
100 m	1/2	1/3	1/4	1/5	1/6	1/7	1/8	1/9
300 m	3/2	1	3/4	3/5	1/2	3/7	3/8	1/3
600 m	3	2	3/2	6/5	1	6/7	3/4	2/3
900 m	9/2	3	9/4	9/5	3/2	9/7	9/8	1

© 2020 The Authors. *Geophysical Prospecting* published by John Wiley & Sons Ltd on behalf of European Association of Geoscientists & Engineers.,

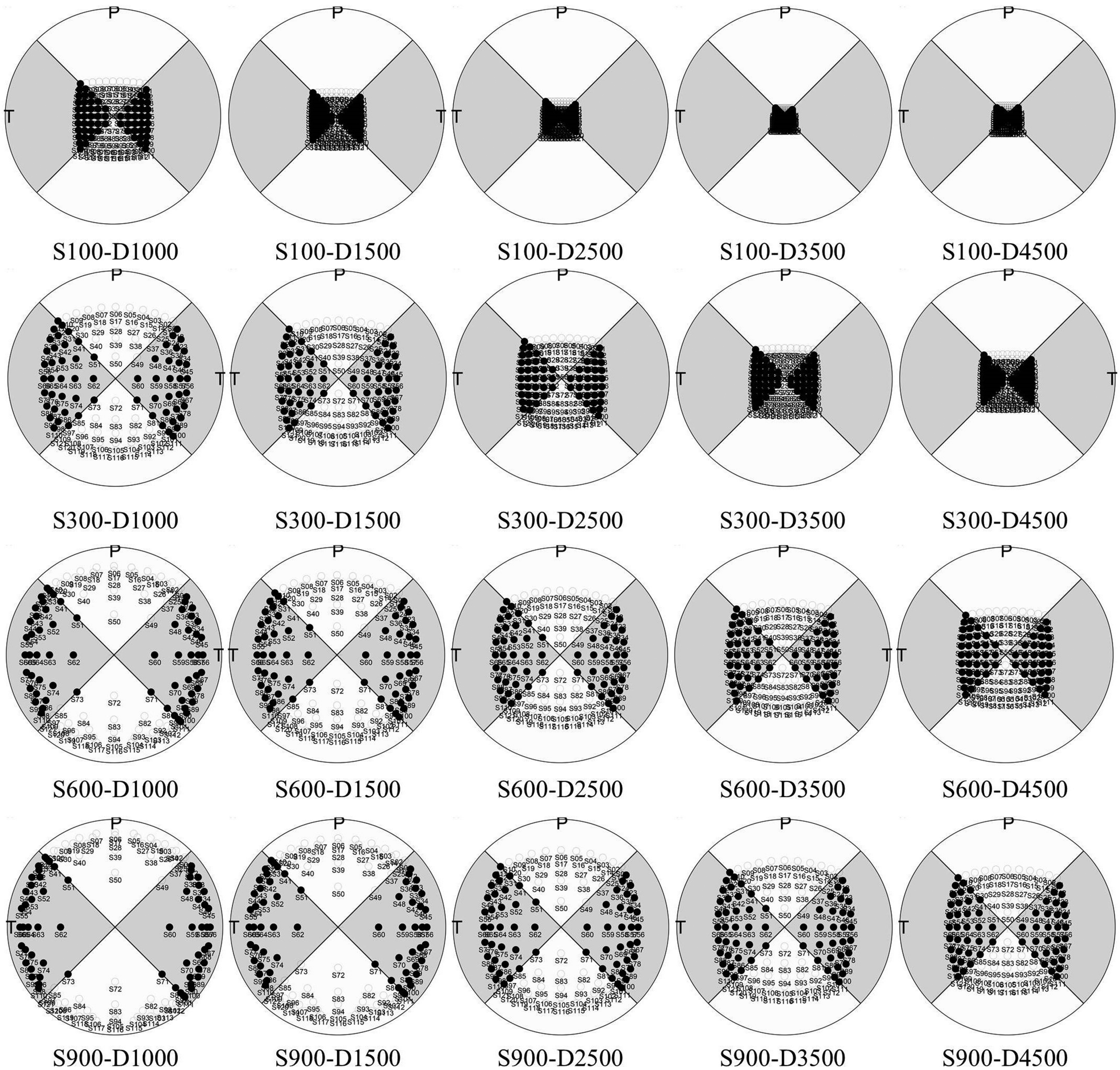

Figure 2 Arrays of 121 sensors with a varying ratio *R* together with the strike-slip focal mechanism projected on the focal sphere. The sensor spacing ranges from 100 m (S100) to 900 m (S900), and depth ranges from 1000 m (D1000) to 4500 m (D4500).

The event magnitude is −1, and the density of the medium is 2700 kg/m^3. The P-wave velocity is 4000 m/s, and the Poisson's ratio is 0.25. Under this Poisson's ratio, the percentages of the double-couple (DC) and non-DC components obtained by the standard moment tensor (MT) decomposition corresponding to different angles α are shown in Table 3 (Vavryčuk, 2001).

In studies of microseismicity associated with hydraulic fracturing, it is important to detect accurately the shear-tensile character of microearthquakes. The amount of shear fracturing in the source can effectively be measured by the DC percentage of MTs. Therefore, we evaluate the accuracy of the MT inversion by calculating uncertainties in the DC percentage as follows:

$$\text{DC error} = \frac{\sum_{i=1}^{n} |\text{DC}_i - \text{DC}_{\text{true}}|}{n}, \tag{8}$$

where the DC error is the average error of n simulations for the same event; DC_i is the DC percentage of the ith realization

© 2020 The Authors. *Geophysical Prospecting* published by John Wiley & Sons Ltd on behalf of European Association of Geoscientists & Engineers., *Geophysical Prospecting*, **68, 2347–2360**

Table 3 Decomposition of moment tensors corresponding to slope angle α (Poisson's ratio is 0.25)

MT Component	$\alpha = 0°$	$\alpha = 10°$	$\alpha = 30°$	$\alpha = 90°$
ISO (%)	0.00	21.48	41.67	55.56
CLVD (%)	0.00	17.18	33.33	44.44
DC (%)	100.00	61.33	25.00	0.00

of random noise and DC_{true} is the DC percentage for the event with synthetic strike, dip, rake and slope angles.

In some simulations, we consider location errors to mimic real situations. Such errors are usually caused by inaccurate picking of arrival times and using an inaccurate velocity model in a location procedure. Instead of fixing a true location of the event, we use a random location of the event inside a box with size of ±50 m (N-S) × ±50 m (W-E) × ±100 m (depth) with the true event location in its centre. The error is twice larger in depth than in the horizontal direction because the surface monitoring does not constrain the event depth very well as shown by many authors (Eisner *et al.*, 2009, 2010a; Janský *et al.*, 2013). Additionally, we perform numerical experiments to study the sensitivity of errors of the MTs on the number of sensors. We calculate MTs using 121 sensors (spacing 600 m, 11 × 11), 49 sensors (spacing 1000 m, 7 × 7) and 16 sensors (spacing 2000 m, 4 × 4) for events with arbitrary focal mechanisms as well as with the strike-slip and dip-slip focal mechanisms. The layouts of sensors projected on the focal sphere are shown in Fig. 3.

RESULTS

Figure 4 shows the double-couple (DC) errors as a function of depth for events with an arbitrary focal mechanism inverted from noisy data recorded at 121 sensors. The sensor spacing ranges from 100 to 900 m (see Fig. 2) and four different slope angles (α = 0°, 10°, 30° and 90°) are assumed. The largest DC errors are observed for spacing of 100 m (Fig. 4, black line) except for the event depth of 1000 m. The DC errors steeply rise with depth of the event for all values of slope α. The increase of the DC errors is also observed for spacing of

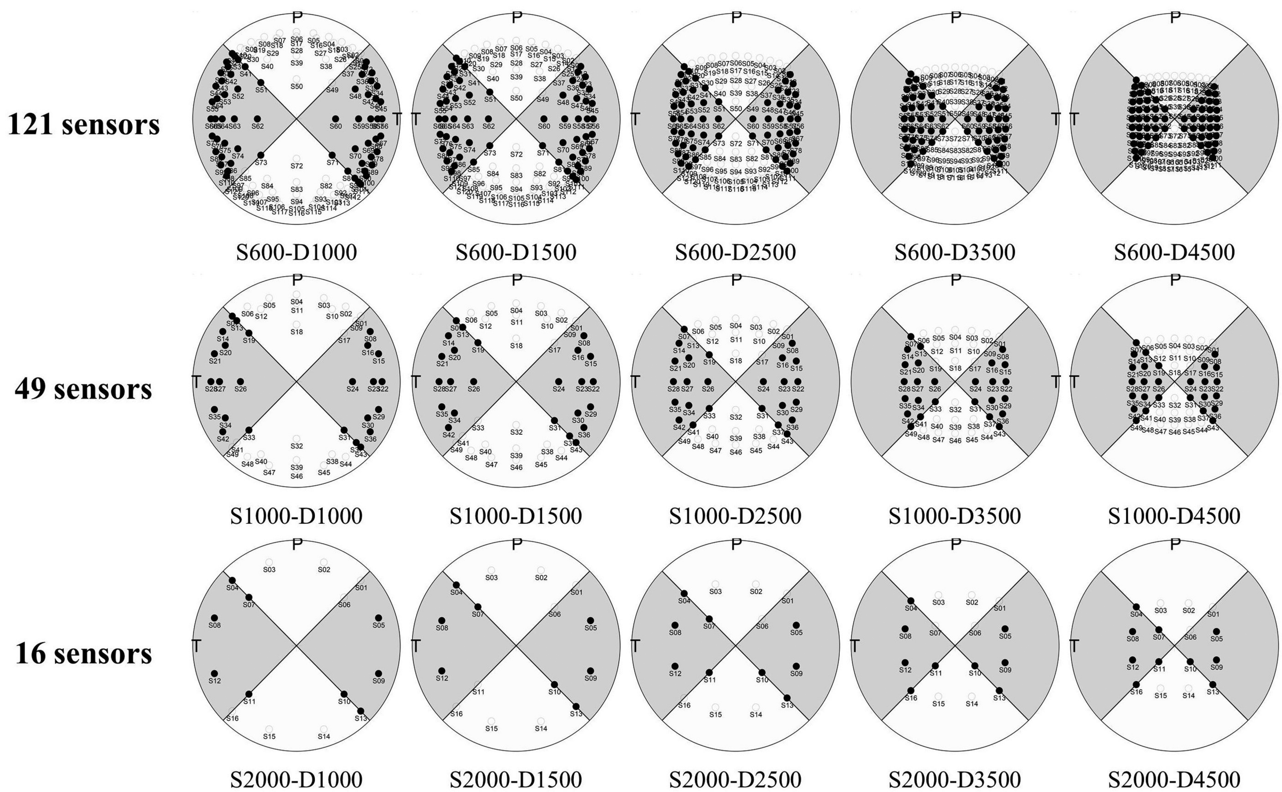

Figure 3 Arrays with a varying number of sensors (121, 49, 16) together with the strike-slip focal mechanism projected on the focal sphere. The sensor spacing ranges from 600 m (S600) to 2000 m (S2000), and depth ranges from 1000 m (D1000) to 4500 m (D4500).

© 2020 The Authors. *Geophysical Prospecting* published by John Wiley & Sons Ltd on behalf of European Association of Geoscientists & Engineers.,

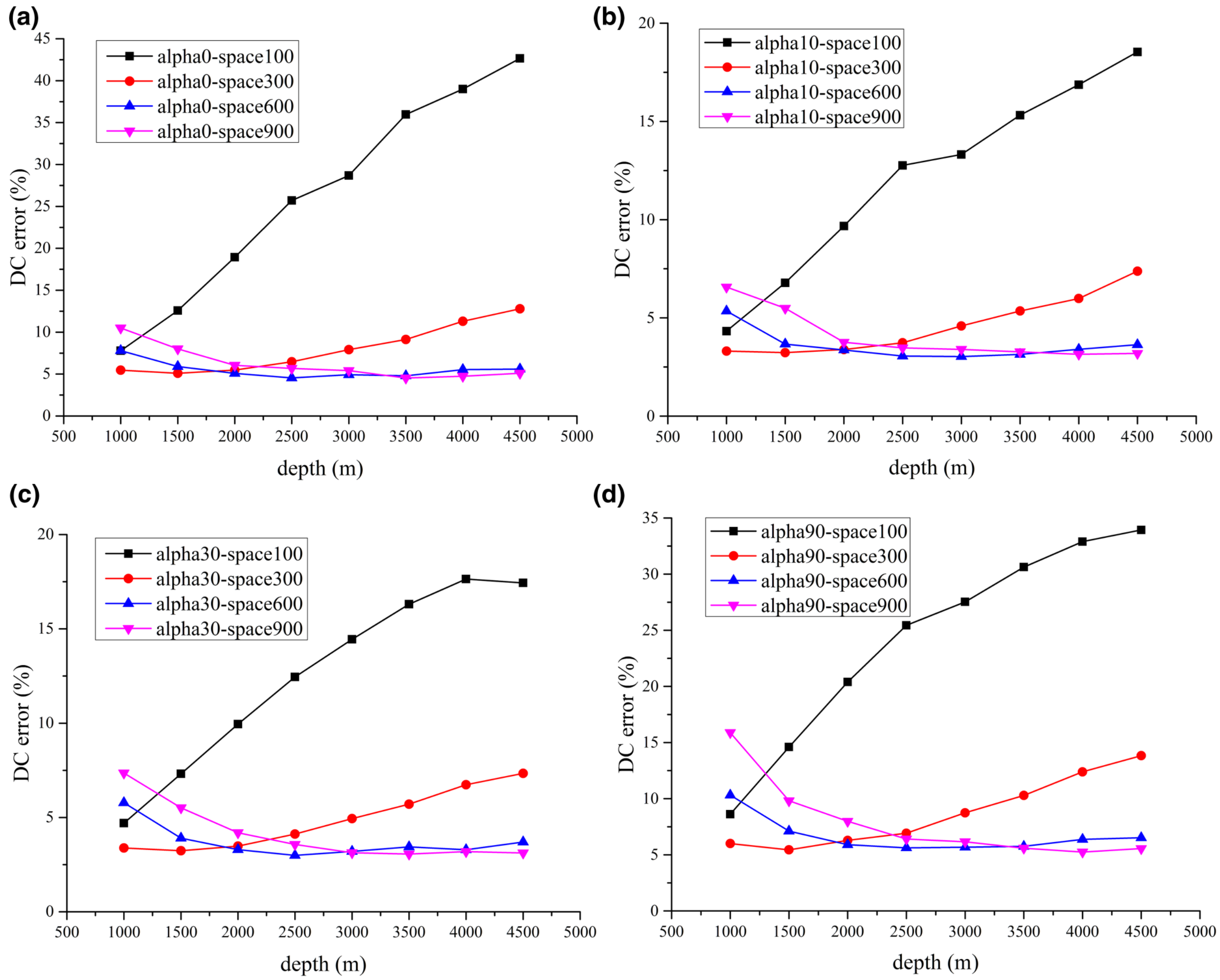

Figure 4 The DC errors for events with a random focal mechanism as a function of the sensor spacing a and depth of the events: (a) $\alpha = 0°$; (b) $\alpha = 10°$; (c) $\alpha = 30°$; (d) $\alpha = 90°$. The input data are contaminated by random noise. The accurate event location is considered.

300 m, but the increase is less prominent than for the 100 m spacing. By contrast, the spacing of 900 m has a trend that is almost completely opposite to spacing of 300 m. For the spacing of 600 m, the DC errors decrease in the depth range from 1000 to 2500 m and slightly increase for depths higher than 2500 m.

In order to understand a complicated behaviour of the DC errors for different spacing of sensors (Fig. 4), we show the DC errors as a function of the offset-to-depth ratio R in Fig. 5. The figure clearly demonstrates that the key factor affecting the DC errors is not the sensor spacing but the ratio R. Regardless of the slope angle α, the DC errors start with a rapid drop, they reach their minimum, and then they increase with increasing R. The values of R, for which the DC errors behave smoothly and are relatively small, are in the range of 0.75–1.5. If R is less than 0.75, the DC errors are quite high and steeply increase with decreasing R. If R is greater than 1.5, the DC errors are moderate and increase slowly with increasing R. Interestingly, the highest accuracy is achieved for $\alpha = 10°$ and 30°. The DC errors for pure shear ($\alpha = 0°$) and pure tensile ($\alpha = 90°$) events are slightly higher, probably due to very special radiation patterns of their focal mechanisms. In addition, the DC errors are affected by the fact that the DC of 100% for the pure shear events and the DC of 0% for the pure tensile events can never be achieved by inverting noisy data.

© 2020 The Authors. *Geophysical Prospecting* published by John Wiley & Sons Ltd on behalf of European Association of Geoscientists & Engineers., *Geophysical Prospecting*, **68**, 2347–2360

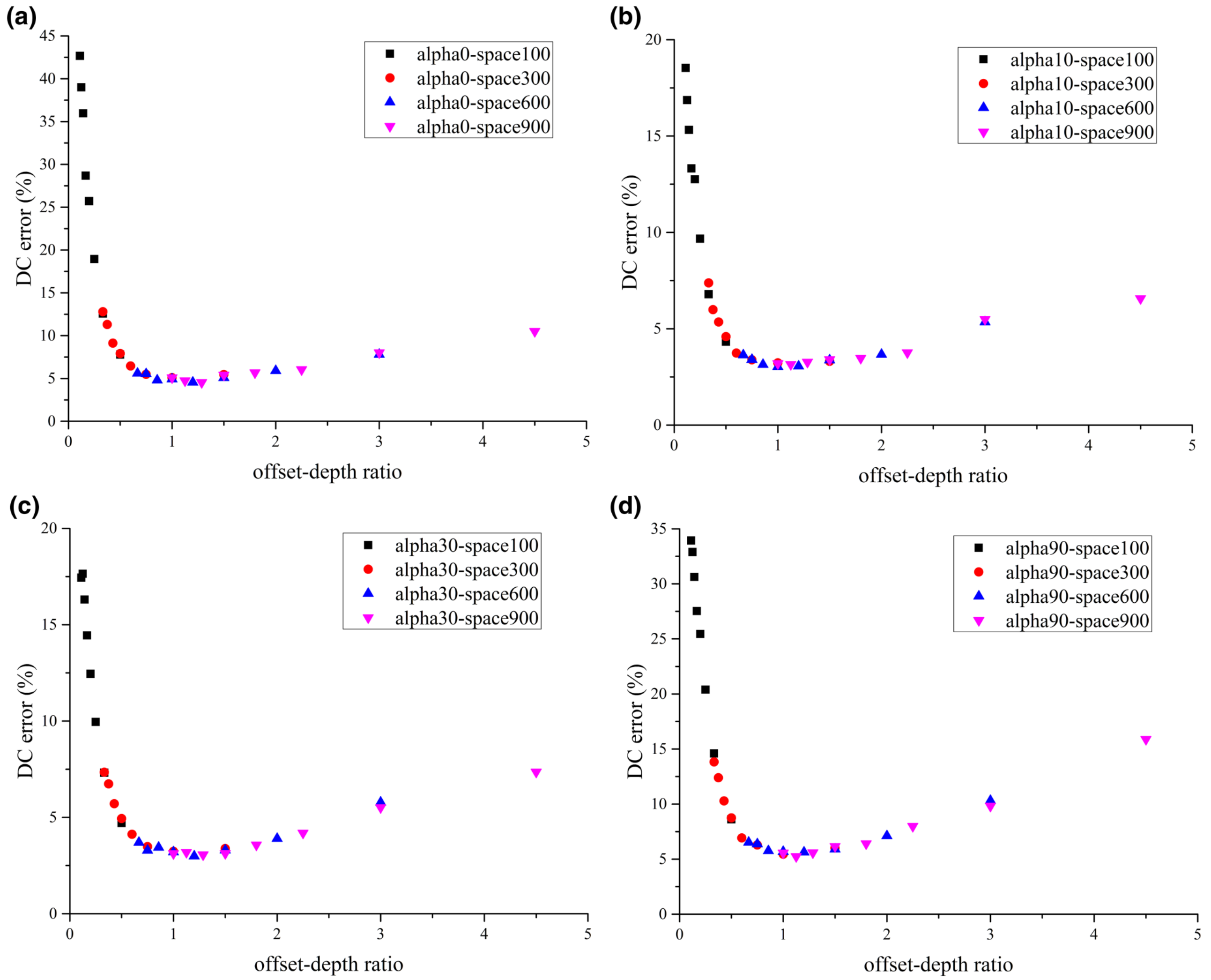

Figure 5 The DC errors for events with a random focal mechanism as a function of sensor spacing a and ratio R: (a) $\alpha = 0°$; (b) $\alpha = 10°$; (c) $\alpha = 30°$; (d) $\alpha = 90°$. The data are contaminated by random noise. The accurate event location is considered.

Figure 6 shows the DC errors as a function of ratio R for events with the pure shear strike-slip (Fig. 6a) and pure shear dip-slip (Fig. 6b) mechanisms. The DC errors for the pure shear strike-slip mechanism (Fig. 6a) are very different from the DC errors shown in Figure 5, in particular, when R is less than 0.75. For R larger than 0.75, the results are similar to those for the events with random focal mechanisms. Such an anomaly is not observed for the pure shear dip-slip mechanism (Fig. 6b), which behaves as the random focal mechanism in the whole interval of ratio R. Also no such anomaly is observed for non-shear strike-slip and dip-slip mechanisms (slope angle of 10°, 30° and 90°), which behave similarly as in Fig. 5. The reason, why the results for the pure shear strike-slip event are different, will be given in the Discussion section.

Next, we conducted tests for arrays with a different number of sensors. Figure 7 shows the DC errors for configurations with 121, 49 and 16 sensors, which recorded noisy data of events with inaccurate locations (noise 10%, N-S: ±50 m, W-E: ±50 m, depth: ±100 m). The events are considered to have a random focal mechanism. All tests indicate that the relationship between R and the DC error is similar. The larger the number of sensors, the lower the DC error and its uncertainty. In the case of 121 sensors, the difference between the DC errors for inaccurate locations (Fig. 7) and accurate locations (Fig. 5, a part consistent with the results shown in Fig. 7) is very small for R within the range of 0.75–1.5. The location errors may cause some fluctuations, but the overall trend is unchanged and the fluctuations are small.

© 2020 The Authors. *Geophysical Prospecting* published by John Wiley & Sons Ltd on behalf of European Association of Geoscientists & Engineers.,

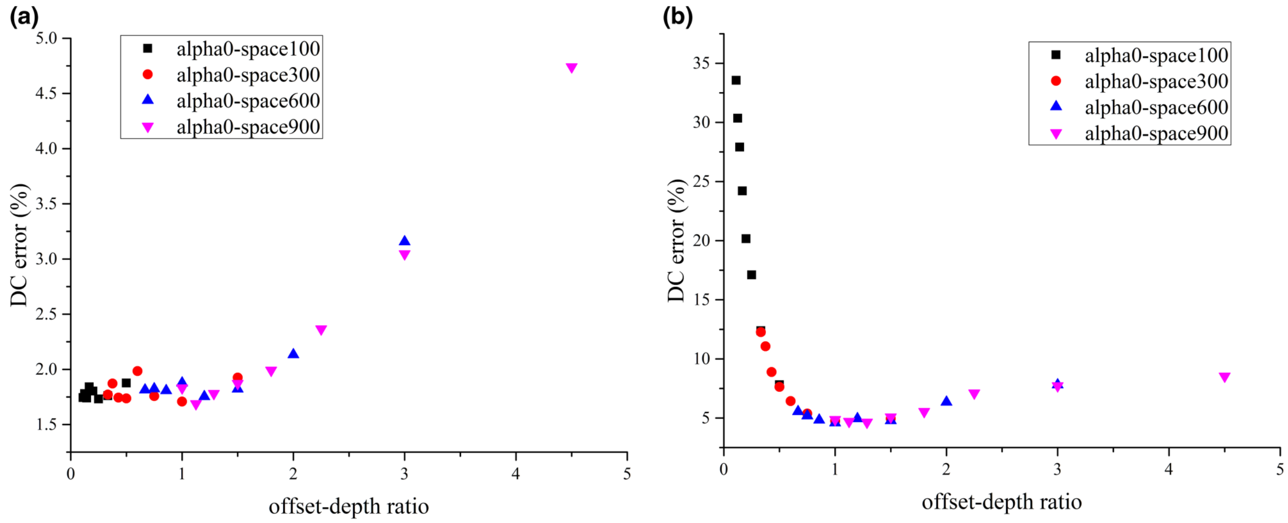

Figure 6 The DC errors for the pure shear strike-slip and dip-slip events as a function of ratio R: (a) strike-slip event, $\alpha = 0°$; (b) dip-slip event, $\alpha = 0°$. The data are contaminated by random noise. The accurate event location is considered. Note the anomal behaviour of the DC errors in plot (a) for $R < 0.75$.

For noisy data and inaccurate locations, the mean DC errors of 121 sensors are always smaller than 6% for R between 0.75 and 1.5. When the number of sensors is 49, which is less than half of 121, DC errors only increase by about 3%. However, the sparse array with 16 sensors only produces large and unstable DC errors in the moment tensors (MTs).

Figure 8 shows the DC errors for events with the pure shear strike-slip and pure shear dip-slip mechanisms. The DC errors of the pure shear strike-slip event are less affected by noise and location errors than those of the dip-slip event. The DC errors for 121 and 49 sensors are very small, only about 3% for the strike-slip event and about 8% for the dip-slip event. Too sparse arrays produce large and unstable DC errors. For large R, the results for the dip-slip event obtained for 121 and 49 sensors are basically the same (Fig. 8b), which looks a bit strange. We will explain this point in the Discussion section.

DISCUSSION

The simulations proved that the offset-to-depth ratio R of the sensor array has a strong effect on the accuracy of inverted moment tensors (MTs). For R between 0.75 and 1.5, the MTs of events could be calculated with a minimum double-couple (DC) error regardless the focal mechanism and tensile angle α. If 121 sensors are used, the DC error varies very slightly for the mentioned interval of R, being higher at most by 1.5% than the minimum DC error. Hence, if the expected depth d of the induced microseismic events is known in hydraulic fracturing experiments, the optimum sensor array should be designed to have the receiver offset comparable to d. If R is too large, the outer sensors of the array are relatively far away from the event location and their positions on the focal sphere are not optimum. Moreover, larger distances between receivers and sources result in higher attenuation of waves, and the signal-to-noise ratio (SNR) may also decrease. As a result, the quality of the signal recorded by sensors might be rather poor, resulting in larger errors in locations and retrieved MTs.

In general, the more sensors, the higher the accuracy of the event locations and of the MT solutions. However, the number of sensors is closely related to the cost of microseismic arrays, which is often limited. If a deployment of more than 100 sensors is not possible and a reduction of sensors is needed, we can still design an array, which yields MTs with a reasonable accuracy. If R is between 0.75 and 1.5, the DC error obtained using 49 regularly spaced sensors is less than 11% irrespective of the focal mechanism and slope angle α. For events with some special focal mechanisms like the strike-slip events, the DC error obtained by using even 16 regularly spaced sensors is less than 6%. If R is greater than 1.5, too sparse sensor arrays lead to large errors and high uncertainties in the MTs.

The very low DC errors for events with the pure shear strike-slip mechanisms (Figs 6a and 8a) can be explained by analysing the P-wave amplitudes recorded by the sensors. We select the 121 sensor array with $R = 1$ and plot the amplitude

© 2020 The Authors. *Geophysical Prospecting* published by John Wiley & Sons Ltd on behalf of European Association of Geoscientists & Engineers.,

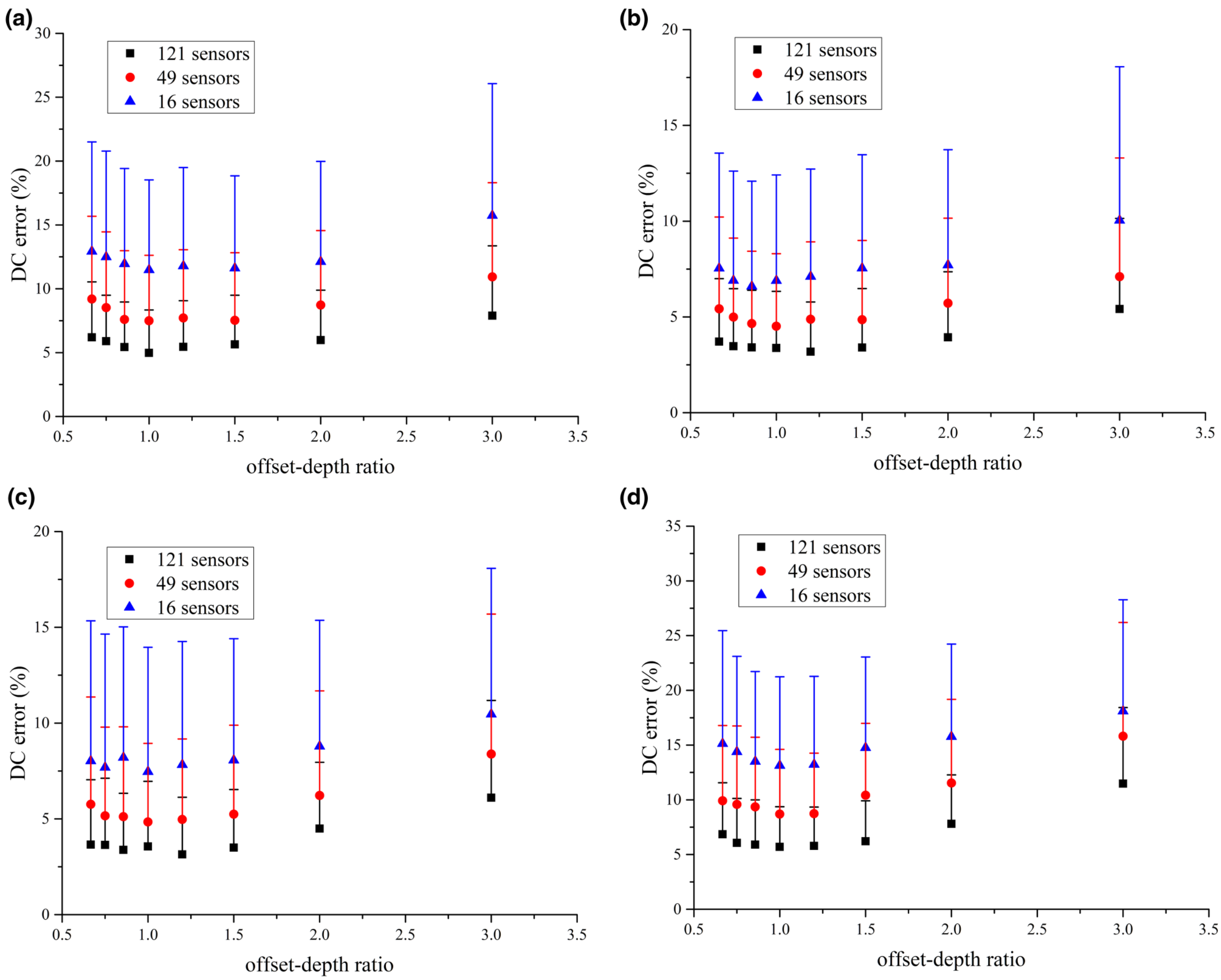

Figure 7 The mean and maximum DC errors for events with random focal mechanisms as a function of ratio *R* for events with inaccurate locations and for noisy data: (a) $\alpha = 0°$; (b) $\alpha = 10°$; (c) $\alpha = 30°$; (d) $\alpha = 90°$. Different sensor configurations are shown in black (121 sensors), red (49 sensors) and blue (16 sensors). The colour markers show the mean DC errors.

distribution for the pure shear strike-slip and dip-slip events (Fig. 9). The analysed strike-slip mechanism is very specific and conveniently oriented with respect to the array because it has two nodal lines perpendicular to each other and the polarities of the amplitudes are opposite on two sides of the nodal lines. In this case, the position of the nodal lines is well constrained even under the influence of noise. The nodal lines are accurately determined also for a very small ratio *R*, which yields generally large errors for events with an arbitrarily oriented focal mechanism. For the pure shear dip-slip mechanism, only one nodal line intersects the array, which leads to larger uncertainties when determining the nodal line position.

Another interesting phenomenon is shown in Figure 8b: if ratio *R* is large (3 or higher), the difference between the DC errors produced for the dip-slip event recorded by arrays with 121 and 49 sensors is small. This indicates that some sensors in the 121-sensor array are redundant and do not contribute to reducing the DC error. For this particular case, the positions of the majority of sensors on the focal sphere are along the circle (see Fig. 2) with a gap for the near-vertical directions. Obviously, such coverage is unfavourable and a high density of sensors in unsuitable directions does not improve the solution. This points to a need of a sufficient number of sensors in near-vertical directions to avoid gaps in the sensor coverage on the focal sphere.

© 2020 The Authors. *Geophysical Prospecting* published by John Wiley & Sons Ltd on behalf of European Association of Geoscientists & Engineers.,

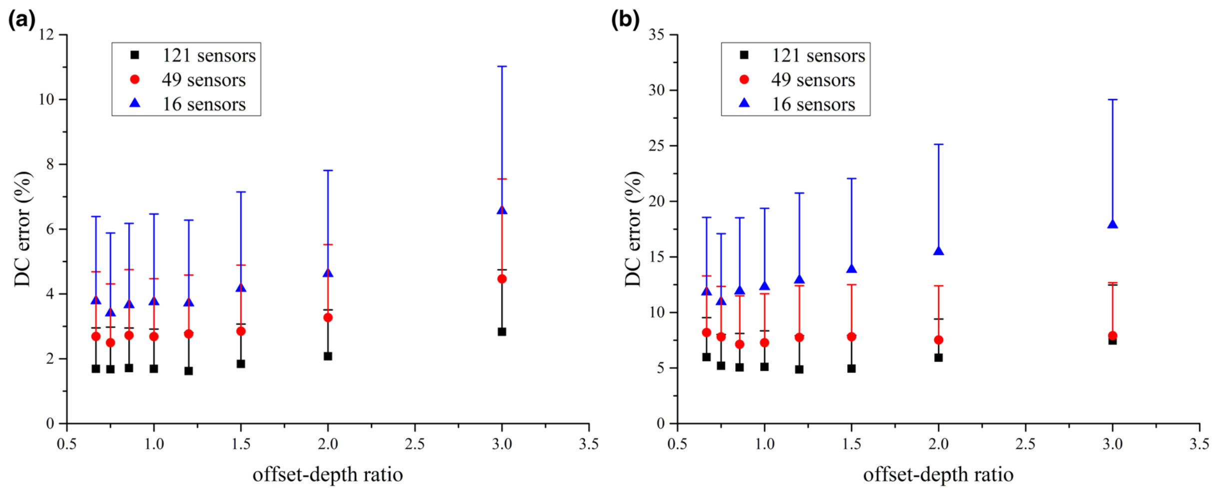

Figure 8 The mean and maximum DC errors as a function of ratio R for the pure shear strike-slip and dip-slip events with inaccurate locations and for noisy data: (a) strike-slip event, $\alpha = 0°$; (b) dip-slip event, $\alpha = 0°$. Different sensor configurations are shown in black (121 sensors), red (49 sensors) and blue (16 sensors). The colour markers show the mean DC errors.

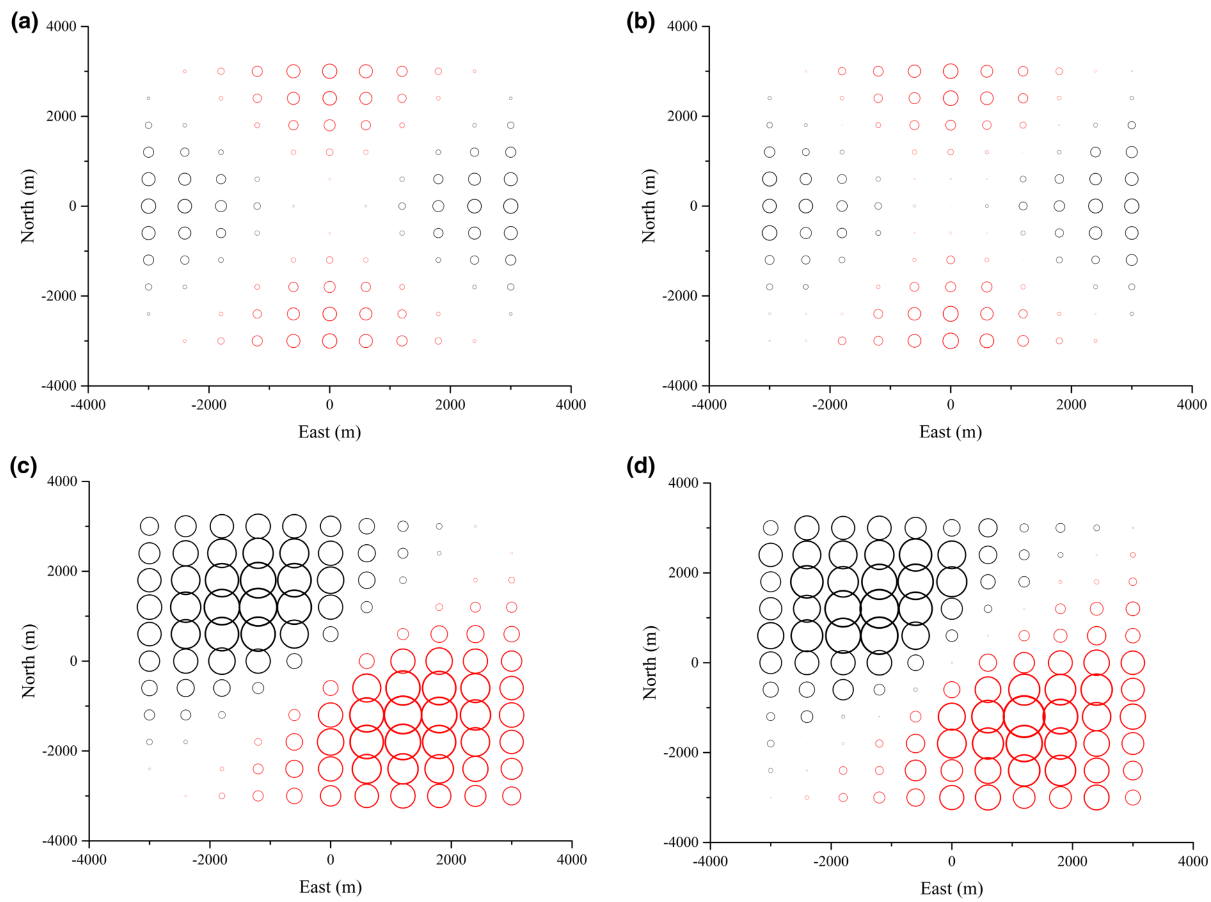

Figure 9 Comparison of the P-wave amplitudes at sensors for noise-free and noisy data for events with the pure shear strike-slip and dip-slip mechanisms: (a) strike-slip event, noise-free; (b) strike-slip event, noisy; (c) dip-slip event, noise-free; (d) dip-slip event, noisy. The circle radius measures the absolute value of the amplitude, the black colour means the positive amplitude, and the red colour means the negative amplitude.

© 2020 The Authors. *Geophysical Prospecting* published by John Wiley & Sons Ltd on behalf of European Association of Geoscientists & Engineers., *Geophysical Prospecting*, **68**, 2347–2360

CONCLUSION

This study shows that the size of the surface arrays and the number of sensors essentially influence the accuracy of the moment tensor (MT) inversion. One of the most important parameters is the offset-to-depth ratio R. If R is set between 0.75 and 1.5, we obtain a highest accuracy of the MTs irrespective of the focal mechanisms and slope angle α characterizing the extent of the tensile fracturing. Reducing the number of sensors leads to higher double-couple (DC) errors of the MTs. Nevertheless, if R is too large (3 or higher), the majority of sensors does not constrain the solution well, because the sensors have an unfavourable position on the focal sphere. Consequently, it might happen that the same accuracy is achieved using a lower number of sensors in this particular case.

A different number of sensors produce different levels of the DC error. The choice, how many sensors to install, depends on the requested accuracy of the MTs and on details in tensile fracturing, which we want to study. The array of 121 sensors with the optimum ratio R is capable to determine the DC percentage with an error less than 6% for events with an arbitrary focal mechanism. This means that the slope angle is determined with the accuracy of a few degrees. The DC error further increases by additional 5% if we use 49 sensors instead of 121 sensors. Hence, the slope angle α is still determined with a high accuracy. Therefore, one should decide, whether an increase of the accuracy is really desirable and installing an array with twice more sensors is cost-effective. Importantly, if a dense array is not designed in an optimum way (e.g., ratio R is too small or too large), it can easily happen that the dense array provides MTs with an accuracy lower than the sparse arrays configured in a more appropriate way.

We focused just on the simplest layout of the surface monitoring systems: the arrays with a regular grid of sensors. In general, the grid arrays are advantageous because of a uniform coverage of the target area by sensors compared to other frequently used configurations such as the circle, star or cross arrays. Obviously, the efficiency to detect the shear-tensile microearthquakes will vary for different sensor layouts and it should be studied in a similar way as presented in this paper.

ACKNOWLEDGEMENTS

We would like to thank the editor and two anonymous reviewers for their helpful comments and suggestions and Grzegorz Kwiatek for his free software support. The work was partially supported by the Grant Agency of the Czech Republic, grant no. 19–06422S, and by the Scholarship provided by the China Scholarship Council to the first author, and by National Natural Science Foundation of China (51934003, 51774020).

ORCID

Yi Ren https://orcid.org/0000-0003-0964-0517
Václav Vavryčuk https://orcid.org/0000-0003-3962-2678

REFERENCES

Anikiev, D., Valenta, J., Staněk, F. and Eisner, L. (2014) Joint location and source mechanism inversion of microseismic events: benchmarking on seismicity induced by hydraulic fracturing. *Geophysical Journal International*, 198(1), 249–258.

Bentz, S., Martínez-Garzón, P., Kwiatek, G., Bohnhoff, M. and Renner, J. (2018) Sensitivity of full moment tensors to data preprocessing and inversion parameters: a case study from the salton sea geothermal field. *Bulletin of the Seismological Society of America*, 108(2), 588–603.

Červený, V. (2001) *Seismic Ray Theory*. Cambridge: Cambridge University Press.

Chambers, K., Kendall, J.M., Brandsberg-Dahl, S. and Rueda, J. (2010) Testing the ability of surface arrays to monitor microseismic activity. *Geophysical Prospecting*, 58(5), 821–830.

Duncan, P.M. (2005) Is there a future for passive seismic? *First Break*, 23(6), 111–115.

Duncan, P.M. and Eisner, L. (2010) Reservoir characterization using surface microseismic monitoring. *Geophysics*, 75(5), 139–146.

Eaton, D.W. and Forouhideh, F. (2011) Solid angles and the impact of receiver-array geometry on microseismic moment-tensor inversion. *Geophysics*, 76(6), WC77–WC85.

Eide, C.H., Schofield, N., Lecomte, I., Buckley, S.J. and Howell, J.A. (2018) Seismic interpretation of sill complexes in sedimentary basins: implications for the sub-sill imaging problem. *Journal of the Geological Society*, 175(2), 193–209.

Eisner, L., Duncan, P.M., Heigl, W.M. and Keller, W.R. (2009) Uncertainties in passive seismic monitoring. *The Leading Edge*, 28(6), 648–655.

Eisner, L., Hulsey, B.J., Duncan, P., Jurick, D., Werner, H. and Keller, W. (2010a) Comparison of surface and borehole locations of induced seismicity. *Geophysical Prospecting*, 58(5), 809–820.

Eisner, L., Williams-Stroud, S., Hill, A., Duncan, P. and Thornton, M. (2010b) Beyond the dots in the box: microseismicity-constrained fracture models for reservoir simulation. *The Leading Edge*, 29(3), 326–333.

Eyre, T.S. and van der Baan, M. (2015) Overview of moment-tensor inversion of microseismic events. *The Leading Edge*, 34(8), 882–888.

Eyre, T.S. and van der Baan, M. (2017) The reliability of microseismic moment-tensor solutions: surface versus borehole monitoring. *Geophysics*, 82(6), KS113–KS125.

Jansky, J., Plicka, V. and Eisner, L. (2013) Feasibility of jointly locating microseismic events with data from surface and downhole receivers. *First Break*, 31(7), 35–71.

© 2020 The Authors. *Geophysical Prospecting* published by John Wiley & Sons Ltd on behalf of European Association of Geoscientists & Engineers.,

Kühn, D. and Vavryčuk, V. (2013) Determination of full moment tensors of microseismic events in a very heterogeneous mining environment. *Tectonophysics*, 589, 33–43.

Kushnir, A., Rozhkov, N. and Varypaev, A. (2013) Statistically-based approach for monitoring of micro-seismic events. *GEM—International Journal on Geomathematics*, 4(2), 201–225.

Kwiatek, G. and Ben-Zion, Y. (2013) Assessment of P and S wave energy radiated from very small shear-tensile seismic events in a deep South African mine. *Journal of Geophysical Research: Solid Earth*, 118(7), 3630–3641.

Kwiatek, G., Martínez-Garzón, P. and Bohnhoff, M. (2016) HybridMT: a MATLAB/shell environment package for seismic moment tensor inversion and refinement. *Seismological Research Letters*, 87(4), 964–976.

Mahdevari, S., Shahriar, K., Sharifzadeh, M. and Tannant, D.D. (2016) Assessment of failure mechanisms in deep longwall faces based on mining-induced seismicity. *Arabian Journal of Geosciences*, 9(18), 709.

Martínez-Garzón, P., Vavryčuk, V., Kwiatek, G. and Bohnhoff, M. (2016) Sensitivity of stress inversion of focal mechanisms to pore pressure changes. *Geophysical Research Letters*, 43(16), 8441–8450.

Maxwell, S.C., Rutledge, J., Jones, R. and Fehler, M. (2010) Petroleum reservoir characterization using downhole microseismic monitoring. *Geophysics*, 75(5), 75A129–75A137.

McLaskey, G.C. and Lockner, D.A. (2018) Shear failure of a granite pin traversing a sawcut fault. *International Journal of Rock Mechanics and Mining Sciences*, 110, 97–110.

Onnis, L. and Carcione, J.M. (2017) A seismic ray tracing method based on Fibonacci search. *Annals of Geophysics*, 60(2), S0220.

Ou, G.B. (2008) Seismological studies for tensile faults. TAO: terrestrial. *Atmospheric and Oceanic Sciences*, 19(5), 4.

Pesicek, J.D., Cieślik, K., Lambert, M.A., Carrillo, P. and Birkelo, B. (2016) Dense surface seismic data confirm non-double-couple source mechanisms induced by hydraulic fracturing induced non-DC source mechanisms. *Geophysics*, 81(6), KS207–KS217.

Rudziński, Ł., Mirek, J. and Lizurek, G. (2017) Identification of seismic doublets occurred on Rudna mine, *Poland. Acta Geophysica*, 65(2), 287–298.

Růžek, B., Vavryčuk, V., Hrubcová, P., Zedník, J. and Celebration Working Group (2003) Crustal anisotropy in the Bohemian Massif, Czech Republic: observations based on central european lithospheric experiment based on refraction (CELEBRATION) 2000. *Journal of Geophysical Research*, 108(B8), 2392. Available at: https://doi.org/10.1029/2002JB002242.

Šílený, J. (2009) Resolution of non-double-couple mechanisms: simulation of hypocenter mislocation and velocity structure mismodeling. *Bulletin of the Seismological Society of America*, 99(4), 2265–2272.

Šílený, J. and Vavryčuk, V. (2000) Approximate retrieval of the point source in anisotropic media: numerical modelling by indirect parametrization of the source. *Geophysical Journal International*, 143, 700–708.

Šílený, J. and Vavryčuk, V. (2002) Can unbiased source be retrieved from anisotropic waveforms by using an isotropic model of the medium? *Tectonophysics*, 356, 125–138.

Staněk, F., Eisner, L. and Moser, T.J. (2014) Stability of source mechanisms inverted from P-wave amplitude microseismic monitoring data acquired at the surface. *Geophysical Prospecting*, 62(3), 475–490.

Staněk, F., Eisner, L. and Vesnaver, A. (2017) Theoretical assessment of the full-moment-tensor resolvability for receiver arrays used in microseismic monitoring. *Acta Geodynamica and Geomaterialia*, 14(2), 235–240.

Stierle, E., Bohnhoff, M. and Vavryčuk, V. (2014b) Resolution of non-double-couple components in the seismic moment tensor using regional networks: 2. Application to aftershocks of the 1999 Mw 7.4 Izmit earthquake. *Geophysical Journal International*, 196(3), 1878–1888.

Stierle, E., Vavryčuk, V., Šílený, J. and Bohnhoff, M. (2014a) Resolution of non-double-couple components in the seismic moment tensor using regional networks: 1. A synthetic case study. *Geophysical Journal International*, 196(3), 1869–1877.

Thornton, M. and Eisner, L. (2011) Uncertainty in surface microseismic monitoring. *SEG Technical Program, Expanded Abstracts*. Tulsa, OK: Society of Exploration Geophysicists, pp. 1524–1528.

Van Der Baan, M., Eaton, D. and Dusseault, M. (2013) Microseismic monitoring developments in hydraulic fracture stimulation. *ISRM International Conference for Effective and Sustainable Hydraulic Fracturing*. Lisbon: International Society for Rock Mechanics and Rock Engineering.

Vavryčuk, V. (1997) Elastodynamic and elastostatic Green tensors for homogeneous weak transversely isotropic media. *Geophysical Journal International*, 130(3), 786–800.

Vavryčuk, V. (2001) Inversion for parameters of tensile earthquakes. *Journal of Geophysical Research: Solid Earth*, 106(B8), 16339–16355.

Vavryčuk, V. (2003a) Parabolic lines and caustics in homogeneous weakly anisotropic solids. *Geophysical Journal International*, 152, 318–334.

Vavryčuk, V. (2003b) Behavior of rays near singularities in anisotropic media. *Physical Review B*, 67, 054105. Available at: https://doi.org/10.1103/PhysRevB.67.054105.

Vavryčuk, V. (2007) On the retrieval of moment tensors from borehole data. *Geophysical Prospecting*, 55, 381–391.

Vavryčuk, V. (2008) Real ray tracing in anisotropic viscoelastic media. *Geophysical Journal International*, 175(2), 617–626.

Vavryčuk, V. (2011) Tensile earthquakes: theory, modeling, and inversion. *Journal of Geophysical Research*, 116(B12), B12320. Available at: https://doi.org/10.1029/2011JB008770.

Vavryčuk, V., Adamová, P., Doubravová, J. and Jakoubková, H. (2017) Moment tensor inversion based on the principal component analysis of waveforms: method and application to microearthquakes in West Bohemia, Czech Republic. *Seismological Research Letters*, 88(5), 1303–1315.

Vernier, J., Gaucher, E., Dasgupta, S.N. and Jervis, M. (2009) Location accuracy of an integrated microseismic monitoring network: a Saudi Arabian case study. *EAGE Workshop on Passive Seismic*, Limassol, Cyprus.

Wessels, S.A., De La Pena, A., Kratz, M., Williams-Stroud, S. and Jbeili, T. (2011) Identifying faults and fractures in unconventional reservoirs through microseismic monitoring. *First break*, 29(7), 99–104.

© 2020 The Authors. *Geophysical Prospecting* published by John Wiley & Sons Ltd on behalf of European Association of Geoscientists & Engineers., *Geophysical Prospecting*, **68, 2347–2360**

Zhang, Y., Eisner, L., Barker, W., Mueller, M.C. and Smith, K. (2011). Consistent imaging of hydraulic fracture treatments from permanent arrays using a calibrated velocity model. *Third EAGE Passive Seismic Workshop-Actively Passive 201*, March 27–30, Athens, Greece.

Zhao, Y., Yang, T., Bohnhoff, M., Zhang, P., Yu, Q., Zhou, J. *et al*. (2018) Study of the rock mass failure process and mechanisms during the transformation from open-pit to underground mining based on microseismic monitoring. *Rock Mechanics and Rock Engineering*, 51(5), 1473–1493.

© 2020 The Authors. *Geophysical Prospecting* published by John Wiley & Sons Ltd on behalf of European Association of Geoscientists & Engineers., *Geophysical Prospecting*, **68**, 2347–2360